EUROPEAN ORGANIZATION FOR NUCLEAR RESEARCH (CERN)

LHCb-PUB-2016-014
EDMS 1627005
1st August 2016

# LHCb Upgraded RICH 1
# Engineering Design Review Report

The LHCb RICH 1 Collaboration

**University of Bristol, Bristol, UK**
M. Adinolfi, J. Kariuki, K. Petridis, J. Rademacker
**University of Cambridge, Cambridge, UK**
P. Garsed, S.A. Wotton
**University of Genoa and INFN, Genoa, Italy**
R. Cardinale, A. Petrolini
**Imperial College, London, UK**
D. Clark, U. Egede, M. McCann, M. Patel, T. Savidge, D. Websdale
**University of Oxford, Oxford, UK**
M. Brock, N. Harnew, M. Tacon
**University of Padova and INFN, Padova, Italy**
M. Benettoni
**Rutherford Appleton Laboratory, Chilton, UK**
A. J. Brummitt, S. Easo, A. Papanestis, S. Ricciardi, F. F. Wilson
**CERN, Geneva, Switzerland**
C. D'Ambrosio, C. Frei, J. He, D. Piedigrossi



**Abstract**

During the Long Shutdown 2 of the LHC, the LHCb collaboration will replace the upstream Ring Imaging Cherenkov detector (RICH 1). The magnetic shield of the current RICH 1 will be modified, new spherical and plane mirrors will be installed and a new gas enclosure will be manufactured. New photon detectors (multianode photomultiplier tubes) will be used and these, together with their readout electronics, require a new mechanical support system. This document describes the new optical arrangement of RICH 1, its engineering design, installation and alignment. A summary of the project schedule and institute responsibilities is provided.

# Contents

# 1 Introduction

The LHCb experiment is undergoing a major upgrade [1], with data-taking expected to start in 2021. Two Ring Imaging Cherenkov (RICH) detectors, RICH 1 and RICH 2, provide particle identification over the ∼2-100 GeV/c momentum range. The upgraded RICH 1 detector [2] has a single radiator, $C_4F_{10}$ gas, and is located upstream of the LHCb spectrometer dipole magnet, shown in Fig 1. It covers an angular acceptance of 250-300 mrad, as for the current RICH 1 [3], and forms a vessel with dimensions in $(x, y, z)$ [1] of approximately 2 m×4 m×1.2 m.

The upgraded RICH 1 is similar to the current RICH 1 in its concept, however changes to the geometrical and optical arrangement will necessitate a re-build of the detector. The optical system will be replaced to increase the image area of the Cherenkov rings and hence reduce the photon occupancy. This will be achieved within the existing magnetic shielding structure, with only relatively minor modifications. A CAD model of the upgraded RICH 1 is shown in Fig. 2.

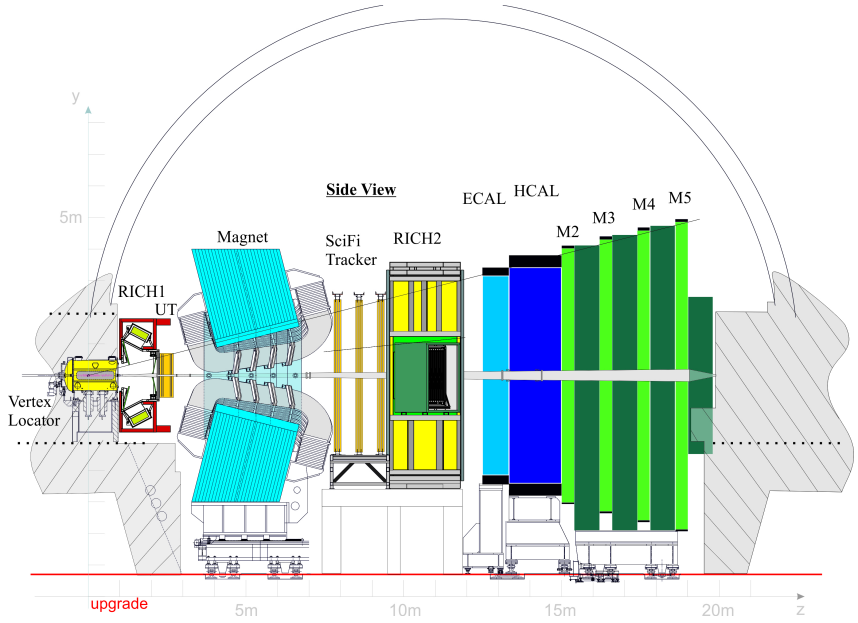


Figure 1: The LHCb upgraded detector [1], showing the location of RICH 1.

The engineering designs for the current RICH 1 detector can be found in the original Engineering Design Report, Ref. [4]. The major changes required for the upgraded RICH 1 detector will be highlighted in this document, and are as follows :

- The aerogel of the current RICH has been removed. Not only has this extended the gas radiator upstream, but RICH 1 has also been extended downstream in $z$

[1]The LHCb $z$-axis follows the beam line which is inclined at 3.6 mrad to the horizontal, and the $y$-axis points upwards, orthogonal to the $z$-axis, with the $x$-axis horizontal.

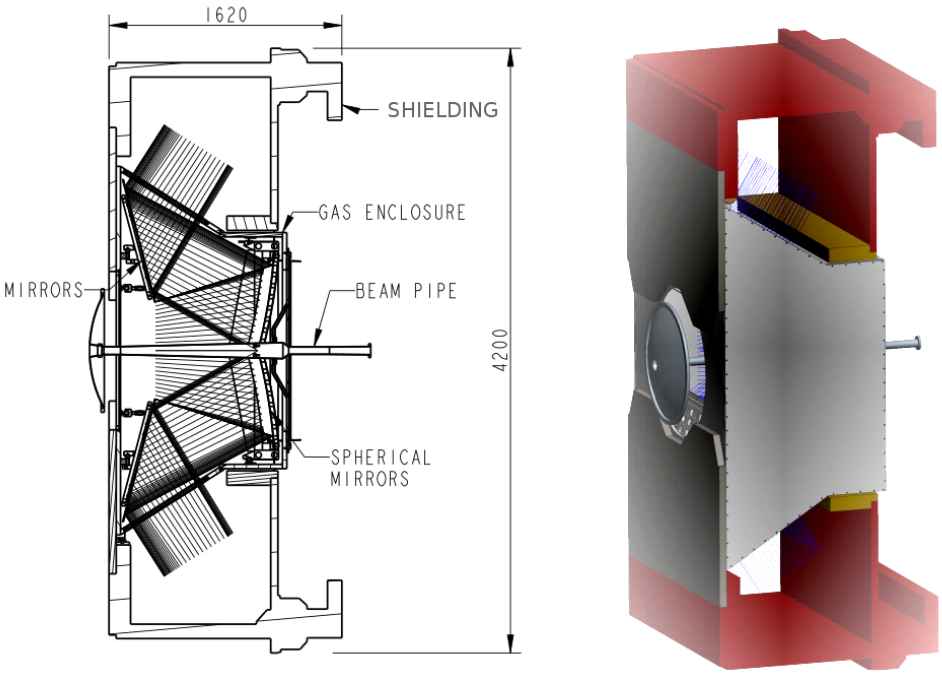


Figure 2: Left: CAD drawing of the upgraded RICH 1 detector, indicating components and dimensions(mm). Right: solid model (the interaction point is to the left of each figure).

by ∼100 mm. This allows the new spherical mirror to be moved downstream thus increasing the total $C_4F_{10}$ radiator length by a further 14%. RICH 1 will be aligned with the LHCb coordinate axes and extend from $z = 985$ mm to $z = 2245$ mm.

- The focusing of Cherenkov light is accomplished using spherical mirrors, tilted to bring the image out of the spectrometer acceptance, and secondary plane mirrors, located above and below the beam. The optics have been modified to spread gas rings over the full detector plane by increasing the radius of curvature of the spherical mirrors from 2710 mm to 3650 mm. All mirrors, plane and spherical, and their mounts, will be replaced. The spherical mirrors lie within the LHCb acceptance and hence will be fabricated in carbon fibre. For the flat mirrors, glass and carbon fibre have been considered. However following an initial quote, carbon fibre seems to be prohibitively expensive, so glass flat mirrors have been adopted as baseline.

- The HPDs in the current RICH 1 will be replaced with multianode photomultipliers (MaPMTs), the 1-inch Hamamatsu R11265. As a consequence of the increased focal length, the photodetector plane must be moved further away from the beam-line. However the area of the photon detector plane remains approximately the same since there is no longer need for coverage from the large-angle aerogel photons.

The MaPMTs are arranged in Elementary Cells (ECs), shown in Fig. 3, which are mounted on columns. RICH 1 will have 22 ECs per column (20 on the two end columns), and each EC contains 4 MaPMTs. The details of the ECs can be found in the corresponding EDR document [5].

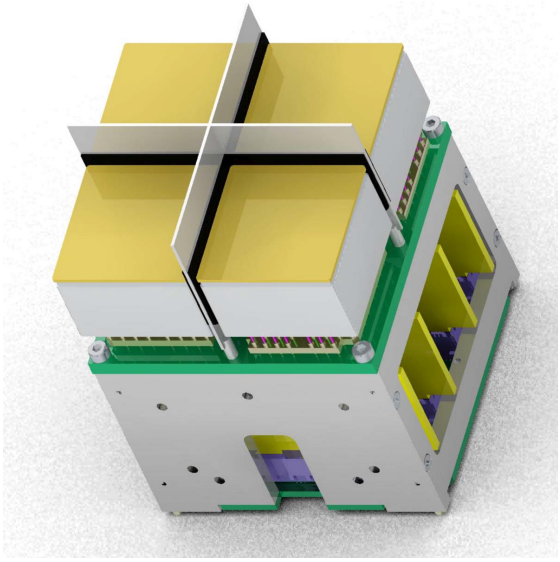

Figure 3: An Elementary Cell; the scale is indicated by the four mounted 1-inch MaPMTs (in orange).

- The relocation of the MaPMT plane is feasible within the current geometric constraints of the iron magnetic shielding, the main structure of which is unchanged. However to retain photon acceptance, the horizontal iron shelf will be reduced in the $z$-dimension by 70 mm, which means that this shelf will need to be replaced.

- The increase in focal length of the spherical mirrors and the extension in $z$ requires a replacement of the Cherenkov gas enclosure, which supports the optical system. The quartz window which isolates the Cherenkov radiator gas from the photon detectors and transmits the photons to the MaPMTs will also be replaced.

- The current HPD photon detector mounting frames inside the magnetic shielding will be replaced to accommodate the MaPMTs. They will be supported from the roof of the magnetic shield on the top, and from the base on the bottom, respectively. Since the photon detector plane has been moved further away from the beamline, the space within the magnetic shield for the photon detectors and readout electronics is now constrained to a volume with dimension about 326 mm transverse to the focal plane. To facilitate the reduced space, an "open geometry" design has been chosen for the photon detector plane, which means the MaPMTs are not surrounded by an external box, and the magnetic shield provides the light and nitrogen gas tightness.

These changes should not affect any conclusions drawn for the tolerance to seismic activity that was previously assessed for the current RICH 1.

The optical system has been optimised using the full LHCb GEANT simulation and the system performance evaluated. The tilt of the spherical mirrors is chosen to be as small as possible to minimise the contribution of emission-point error to the Cherenkov angle resolution. The plane mirrors, located just outside the geometrical acceptance, are tilted such that the centre of the MaPMT plane is approximately positioned to maximise the space available behind it in order to house the MaPMT electronics and services. The geometry resulting from this optimisation process is shown in Fig 4.

Minor changes of the optics with respect to the TDR design [2] were implemented, in accordance with the evolution of the engineering design. In order to provide sufficient space for the readout boards behind the MaPMT array inside the magnetic shielding, the photodetector plane was moved, normal to the plane and towards the beamline, with respect to the TDR location, thus reducing the optical path length by 100 mm. The corresponding redesign of the optics now results in the spherical mirror having a radius of curvature of 3650 mm.

The remainder of this EDR report will describe the engineering designs of the various RICH 1 components. Section 2 describes the magnetic shield modifications. The spherical and flat mirrors and their mounting systems are discussed in Section 3. Modifications to the gas enclosure and photon funnel are described in Section 4. The mechanics of the MaPMT region, the MaPMT mountings and the cooling are discussed in Section 5. The exit and entrance windows and the seal to the beam pipe are described in Section 6. The procedures for installation, alignment and survey of RICH 1 are discussed in Section 7. The overall project organisation, including the schedule and division of tasks between the international collaborators, is detailed in Section 8. Finally, RICH 1 cooling and the radiation considerations and testing are outlined in Appendix A and Appendix B, respectively.

# 2 Magnetic Shield

As the MaPMTs are sensitive to the magnetic environment, the photon detector region is surrounded by an iron structure that reduces the effect of the magnetic fringe field from the LHCb dipole. This shield is dual purpose as it is also used as the mounting structure for the gas enclosure and photon detector assembly. Details of the magnetic shield configuration can be found in Ref. [4].

The existing shielding, while optimised for the current RICH 1, will remain largely unaltered. However, the increase in radiator gas length leads to photons that will be blocked from reaching the photon detectors by the current shelf, as demonstrated in Fig. 5. A much smaller fraction is blocked by the flat mirror extending into the photon acceptance. The shelf is removable and will be replaced by a new shelf which, together with the gas enclosure, will be fully out of the acceptance. The new shelf will be 70 mm (16%) shorter in the $z$ dimension, all other dimensions remaining the same. The primary mounting points

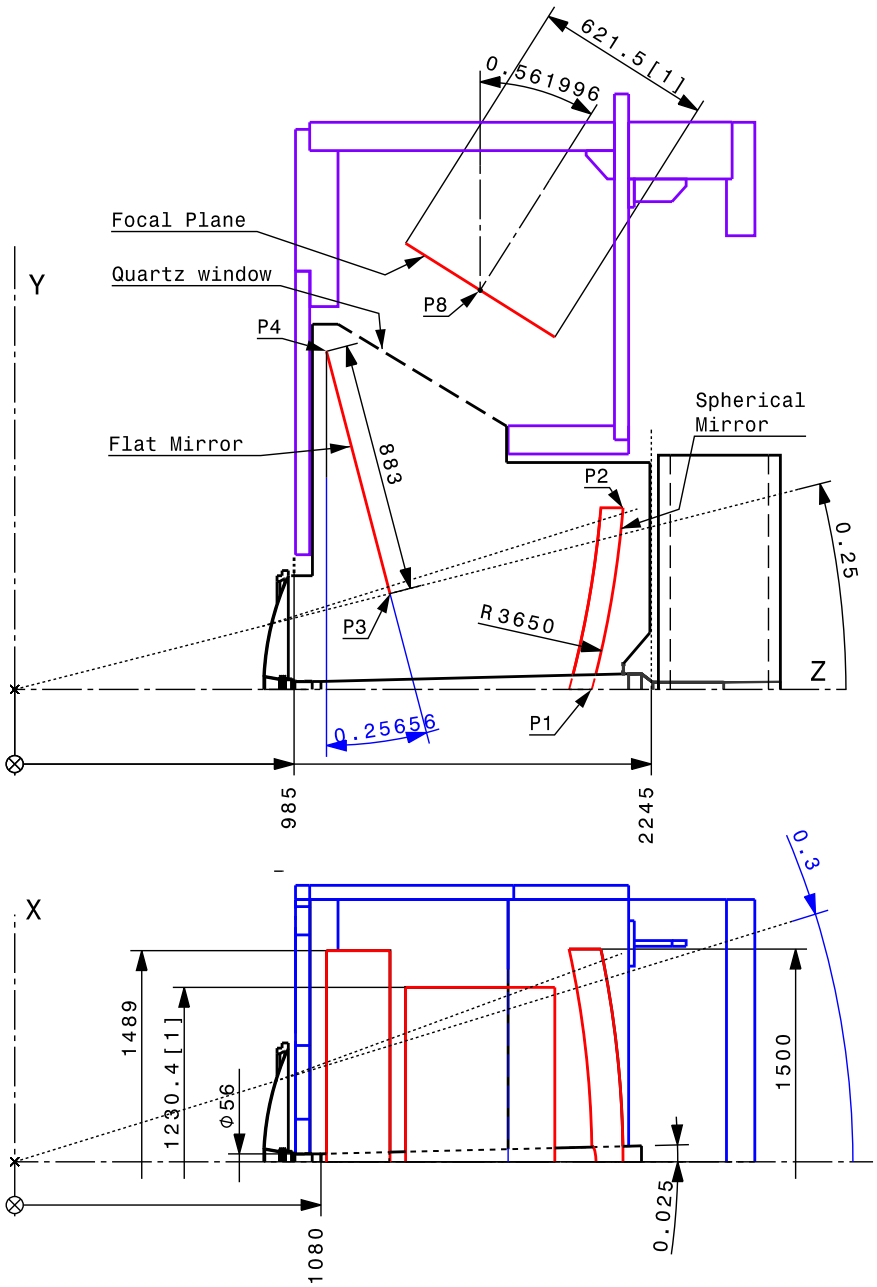


Mirror, center of curvature: X = 0 mm, Y = 932.89711 mm, Z = -1493.28601 mm.
P1: X = 0 mm, Y = 0 mm, (Z = 2035.482 mm).
P2: X = 0 mm, Y = 640.706 mm, (Z = 2145.001 mm).
P3: Y = 337.89575 mm, Z = 1323.30699 mm.
P4: (Y = 1191.994 mm), (Z = 1099.242 mm).
P8: Y = 1407.716 mm, Z = 1641.417 mm.
Limit Z = 2245 mm.
[1]: The size of the photon detector plane is based on:
- The photon detectors (MaPMTs) are assembled on the Elementary Cell.
  The Elementary Cell includes 2x2 photon detectors with a pitch of 28 mm.
- The Elementary Cells are assembled on a column.
  A column is composed of 22 Elementary Cells with pitches of 56 mm.
- The column are assembled with a pitch of 56.5 mm.
  Each photon detector assembly is made of 11 columns.
- The total number of photon detectors: 1920 (16 photon detectors less in the periphery).

RICH1 Upgrade - Optical Layout. Christoph Frei. EDMS-1390002-v2, CF160401-1050 (ST0516168_01-a.03)



Figure 4: A schematic diagram showing the RICH 1 optics: (a) $y - z$ view (b) $x - z$ view.

of the gas enclosure are on the shelf of the lower shield and the locations are dictated by the design of the new gas enclosure. As the MaPMTs are less sensitive to magnetic fields [6] and are significantly further from the shelf than the current HPDs, the reduction in shelf size is not expected to result in a magnetic field that would degrade the MaPMT performance.

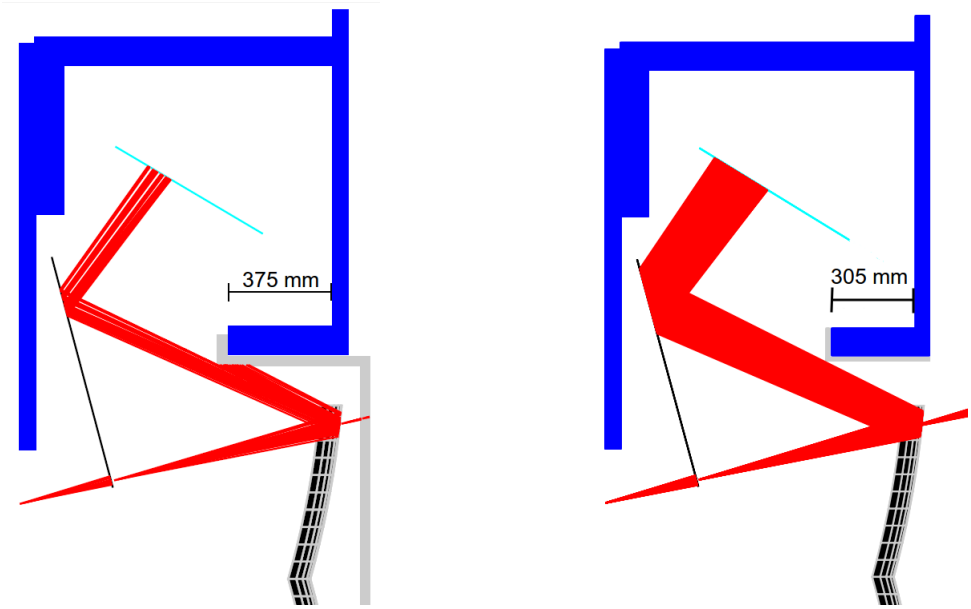


Figure 5: (Left) The ray-traced paths of photons (red) generated by extremal tracks through the upgraded optical elements, with the current magnetic shielding (blue), and gas enclosure (grey). A significant fraction of the most extreme photons are blocked by the current shelf. (Right) The same ray-traced paths with the shelf shaved by 70 mm.

It is expected that no further substantial modification of the shielding will be required. However, alternatives have been investigated to improve access to the MaPMT arrays:

1. Doors could be made which conform to the current dimensions to replace the bolted side panels, but with the service exit altered to better match the routing from the new focal plane.

2. Increasing the $x$ dimension of the shielding by 200 mm by adding iron strips to offset the doors has been studied and shown to be feasible.

Existing internal mounting points will be used where possible, but there will also need to be minor changes to add new mounting holes inside the shielding, which will be added *in situ*. As the shielding will be providing a light-tight environment, the new internal surfaces will be cleaned and coated with a non-reflective paint. It is not foreseen that this will require specialist coatings.

# 3 Spherical and flat mirrors

## 3.1 Spherical mirrors

Four tilted CFRP (Carbon Fibre Reinforced Polymer) spherical mirrors of 740 mm (width) by 650 mm (height) and a radius of curvature of 3650 mm are positioned in four quadrants, centred on the beampipe. The anticipated mirror thickness of 33 mm is close to that of the existing RICH 1 mirrors. Each mirror is supported at three of its corners using spherical rod end adjusters bolted to a CFRP frame made from a 2 inch square tubular structure. This mounting configuration allows for a mirror alignment with a precision of a few tenths of a mrad, as for the existing RICH 1 mirrors. The fourth (inner) corner of each mirror has a quarter-circle cutout to accommodate the beampipe with a clearance of ∼12 mm. Figure 6 shows the spherical mirror assembly.

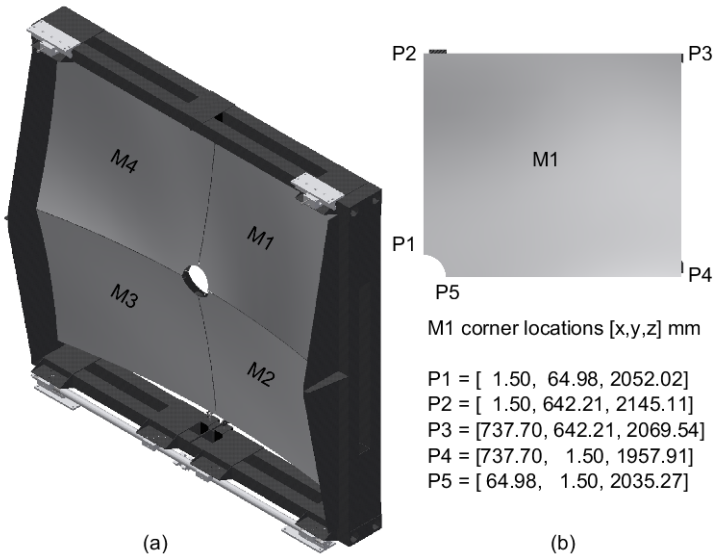


Figure 6: (a) CAD model of the spherical mirror assembly, and (b) M1 mirror corner locations in $(x, y, z)$. The mirror corner locations are symmetric about the $x$ and $y$ axes.

The CFRP frame separates along the vertical axis into two C-like halves, which each support two mirrors positioned vertically. A pre-alignment, which is performed remotely, is required to pair the two top (bottom) mirrors to form one spherical surface pointing to the same top (bottom) centre-of-curvature. A mirror-to-mirror separation distance of 3 mm is used to allow for a safe alignment and to accommodate small deformations. During storage and transportation, each CFRP half frame with its aligned mirrors is safely secured in precision-machined handling boxes. The global position of the CFRP frame and mirror corners, from a fixed reference in the gas enclosure, is then aligned *in situ*. Each CFRP half-frame with its pre-aligned mirrors, weighing ∼10 kg, is bolted to V-blocks which sit on a cylindrical load rail bolted to the floor of the gas enclosure. This allows for installation through the opened side panels of the gas enclosure using temporary rails,

and positioning of the CFRP frame horizontally. Each CFRP half-frame section is secured to a short flat rail, bolted to the ceiling of the gas enclosure, containing a fine adjustment screw. A 1/8 turn of the screw changes the CFRP frame tilt angle relative to the beamline by ∼0.07 mrad. The CFRP half-frame structures are joined at the centre, above and below the beampipe. After final adjustments, the aligned spherical mirror assembly is secured at its two bottom corners sitting on the load rail and one top corner fastened to a short flat rail using a fine adjustment screw.

Static and modal finite element computations were performed using the Autodesk Inventor software to predict the structural performance of the spherical mirrors and support structure. A single spherical mirror was investigated under self-weight loading and constrained at its supports. The results show the maximum stress corresponds to a value of the Factor of Safety (FoS) >10, indicating structural failure of the mirror due to static loading is extremely unlikely. The maximum displacement of the mirror is ∼6.2 $\mu$m and occurs at the corner with the beampipe cutout. The lowest natural frequency is ∼113 Hz. The gas enclosure is exposed to only low amplitude background oscillations within the cavern floor, with frequencies below 5 Hz. These are unlikely to affect the structural rigidity of the mirror structures.

Finite element analysis of the mirror-and-self-weight loaded CFRP frame constrained at the rail mounts has been performed. The results show the highest stresses are very localised, occurring at the mirror adjuster supports and corresponding to FoS values of ∼3. These stresses are likely to be locally redistributed by the spherical bearing design of the mirror adjusters to establish equilibrium. The remaining stresses correspond to FoS values >10, indicating structural failure of the CFRP frame or yielding of the metallic rails and mounts is highly unlikely. The maximum displacement occurs at the top corner of the CFRP frame unfastened from the short flat rail after alignment, and is ∼0.072 mm. Design optimisation of the support structure will be performed to reduce the maximum displacement of the assembly. The lowest natural frequency is ∼23 Hz and is unlikely to pose a problem.

## 3.2 Flat mirrors

Figure 7 shows the flat mirror assembly. Sixteen flat glass mirrors, each of dimensions 370 mm (width) by 440 mm (height) and a radius of curvature > 600 m are assembled into two inclined planes of eight mirrors, each positioned above and below the beampipe. The thickness of the glass mirrors is currently set at 6 mm, with the potential to increase to 8 mm, depending on manufacturing capabilities. Each mirror is bonded at its centre to a polycarbonate mount with a 3-point precision adjustment system replicated from the existing RICH 1 mirror assembly. A 1/8 turn of a fine adjustment screw causes a translation of ∼6.3 $\mu$m normal to the mirror plane, and tilt of ∼0.1 mrad about a designated pivot screw. The polycarbonate mounts are bolted into machined pockets on four rigid 1-inch thick aluminium support frames. Each frame supports four mirrors positioned in a rectangular pattern, and forms half a mirror plane. The support frames are positioned outside the detector acceptance and therefore do not need to be lightweight. A polycarbonate ring

centred on each mirror is bonded over a larger area than the polycarbonate mounts. This ring is secured to the support frame to retain the mirror in the case that the bond of the polycarbonate mount fails.

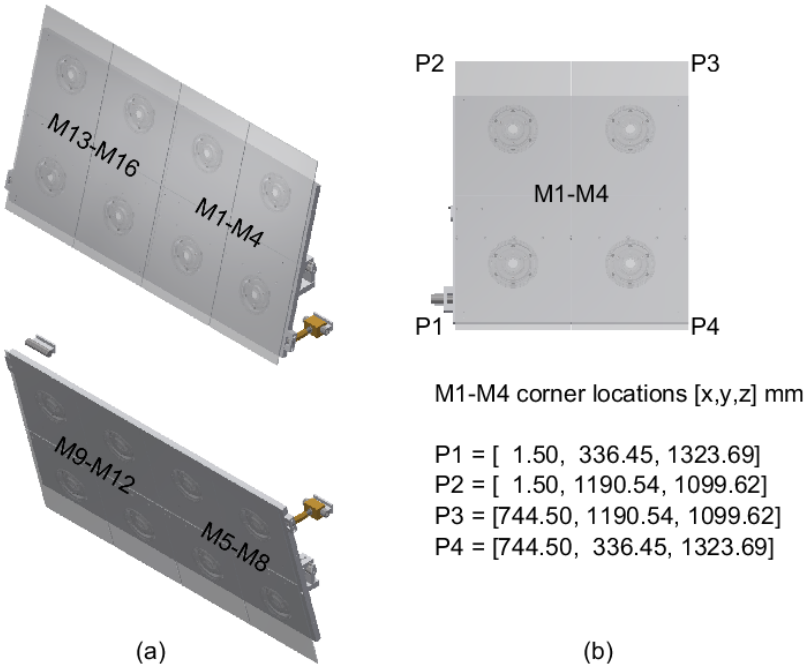


Figure 7: (a) CAD model of the flat mirror assembly, and (b) M1-M4 mirror corner locations in $((x, y, z)$. The mirror corner locations are symmetric about the $x$ and $y$ axes.

A pre-alignment performed remotely is required to pair the two top (bottom) half mirror planes to form a single plane parallel to both support frames pointing to the top (bottom) photon detector plane. A mirror-to-mirror separation distance of 3 mm is used to allow safe alignment and accommodate small deformations. This results in $\sim$1% loss in active reflective surface. During storage and transportation, each support frame with its pre-aligned mirrors is safely secured in precision-machined handling boxes. The global position of the support frames, from a fixed reference in the gas enclosure, is then aligned *in situ*. Each support frame with its pre-aligned mirrors, weighing $\sim$40 kg, is bolted to V-blocks which sit on a load rail bolted to the front panel of the gas enclosure. A controlled procedure incorporating elements to protect the beampipe is followed when installing each support frame sub-assembly through the opened side panels of the gas enclosure using temporary rails. Flat, 1-inch thick aluminium bars positioned 5 mm below the load rails are bolted to each support frame to prevent detachment of the mirror assembly in the event of shocks or seismic tremors. A fine adjustment rod-coupler attached to each support frame is fastened to a short rail bolted to the front panel of the gas enclosure. A 1/8 turn of the coupler changes the mirror plane angle relative to the beamline by $\sim$0.24 mrad. The two support frame pairs are each joined at the centre, above and below the beampipe. After final adjustments, each aligned flat mirror plane assembly is secured at its ends

sitting on the load rail and at one corner fastened to a short rail using a fine adjustment rod-coupler.

Finite element analysis of the upper and lower mirror plane assemblies under self-weight loading and constrained at the rail mounts has been performed. The results show the highest stresses are very localised, occur in the aluminium V-blocks, and corresponding to FoS values of ∼8. During static loading of a ductile material such as aluminium, the material would yield locally in regions of high stress, redistributing the stress and establishing equilibrium. The remaining stresses correspond to FoS values >10, indicating yielding of the metallic structures is very unlikely. The maximum displacement is ∼0.12 mm and occurs at the corner of the mirror plane where a fine adjustment rod-coupler is unfastened from the short rail. The lowest natural frequency is ∼30 Hz and is unlikely to pose a problem.

# 4 Gas enclosure and MaPMT interface

The major functions of the gas enclosure are to contain the RICH 1 $C_4F_{10}$ gas radiator, to support the mirrors and to exclude light. The requirements are the same as the current gas enclosure so the structure is similar: basically a 30 mm thick tapered aluminium box. The current gas enclosure [4] was constructed as a welded assembly with post-weld machining to achieve the sub-millimetre accuracy required for the mirror mounts. This proved problematic since welding distortions were experienced which exceeded 5 mm. The new design is therefore a structure constructed from bolted plates, with gas tightness achieved using bonding. Currently it is envisaged that bonding will be by Hylomar semi-liquid sealant to allow the enclosure to be taken apart and reassembled if required. No concerns with sealing have arisen during testing, however if subsequent radiation testing uncovers problems, an epoxy bond will be used. This is a proven technology but does not allow easy disassembly.

The major changes to the RICH 1 gas enclosure dimensions are shown in the drawings of Fig. 8. To accommodate the upgraded optical design the gas enclosure length is increased in $z$ from 1087 mm to 1187 mm. As described in Section 2, the magnetic shielding shelf length is reduced by 70 mm and the internal edge bevelled locally reducing the thickness of the gas enclosure to about 8 mm. The face of the enclosure containing the quartz window (which transmits photons to the MaPMT plane) is adjusted to match the changed angle of the focal plane so the angle the window makes to the $x$-$y$ plane changes from 62.6° to 57.8°. This changes the height of the front of the gas enclosure from 2440 mm to 2560 mm which necessitates a change to the front mounts of the gas enclosure to reduce height but no changes are required on the iron shielding where they are fitted. The rear mounts are unchanged.

The size of the quartz window is increased from 1340 mm × 554 mm to 1410 mm × 645 mm. Quartz of this size can be fabricated but not coated so the window is divided into three panes bonded together (as for the current window) by a slow-cure epoxy. This assembly is bonded into an aluminium frame for handling and this frame will be bolted to

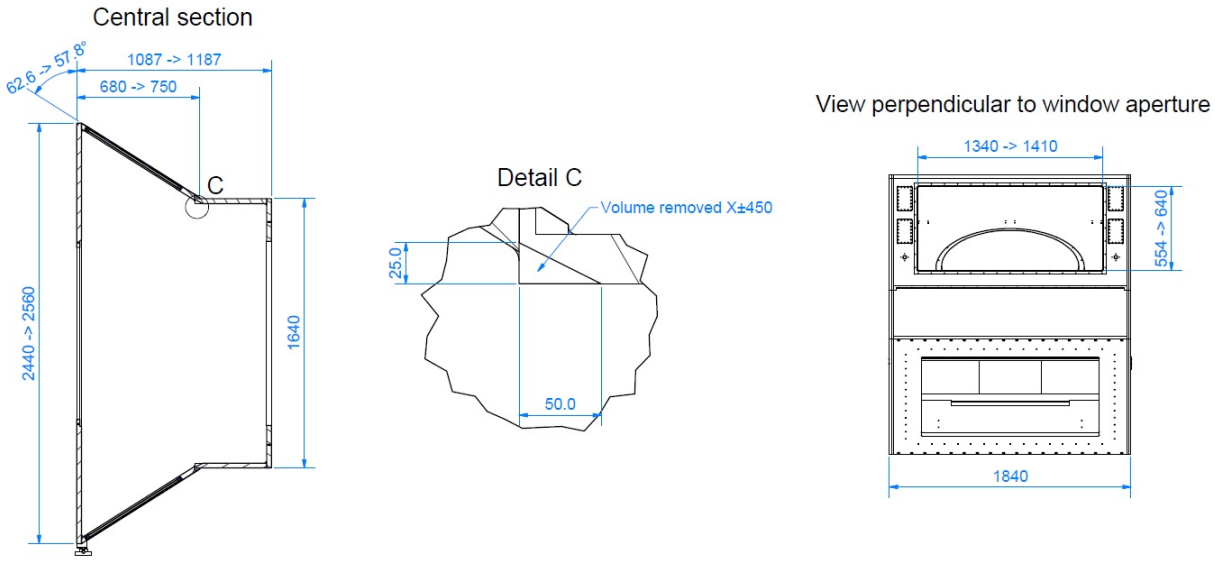


Figure 8: (Left) The $y$-$z$ view of the gas enclosure showing the changes to the gas enclosure dimensions and angles; (Centre) The details of the bevelled edge at the interface of the magnetic shielding shelf; (Right) The view along the normal to the quartz window aperture; the semicircular object is the view of the entrance window through the quartz window aperture.

the gas enclosure with an O-ring to seal the frame to the gas enclosure.

FEA analyses, demonstrated in Fig. 9, show that under gravity and a typical internal pressure difference of 3 mbar, the peak displacement is 39 $\mu$m. Displacement at the mirror mounting points is less than 10 $\mu$m.

The face of the gas enclosure is attached to the enclosure containing the MaPMTs via

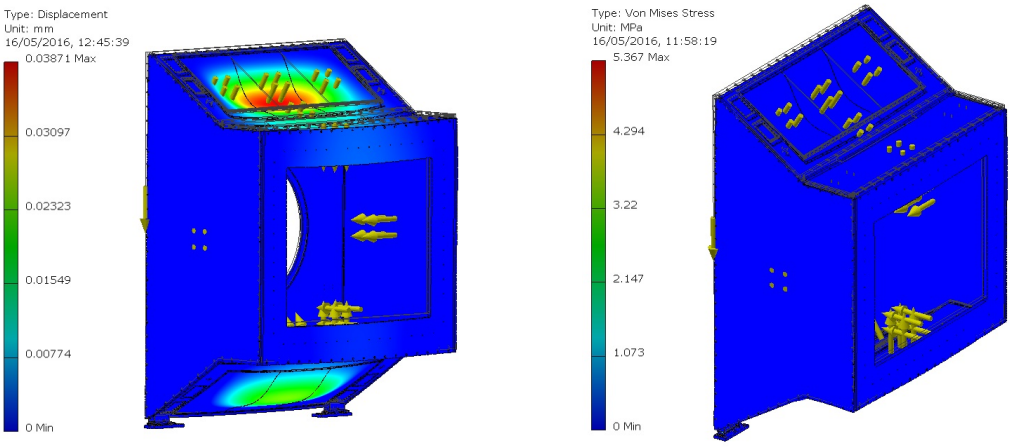


Figure 9: Finite element analysis of the gas enclosure.

the so-called photon funnel, which provides a light-tight interface on the MaPMT side of the quartz window. The photon funnel is constructed as a simple rigid tube made up of four aluminium channel sections. The detailed interface is shown in Fig. 10. Sealing is achieved using a double strip seal with a cross section of 4 mm × 2 mm in the compressed state. The seal should be of soft, closed cell, EPDM foam rubber 4 mm × 4 mm in the uncompressed state allowing it to accommodate large positional mismatches between the gas enclosure and the MaPMT enclosure.

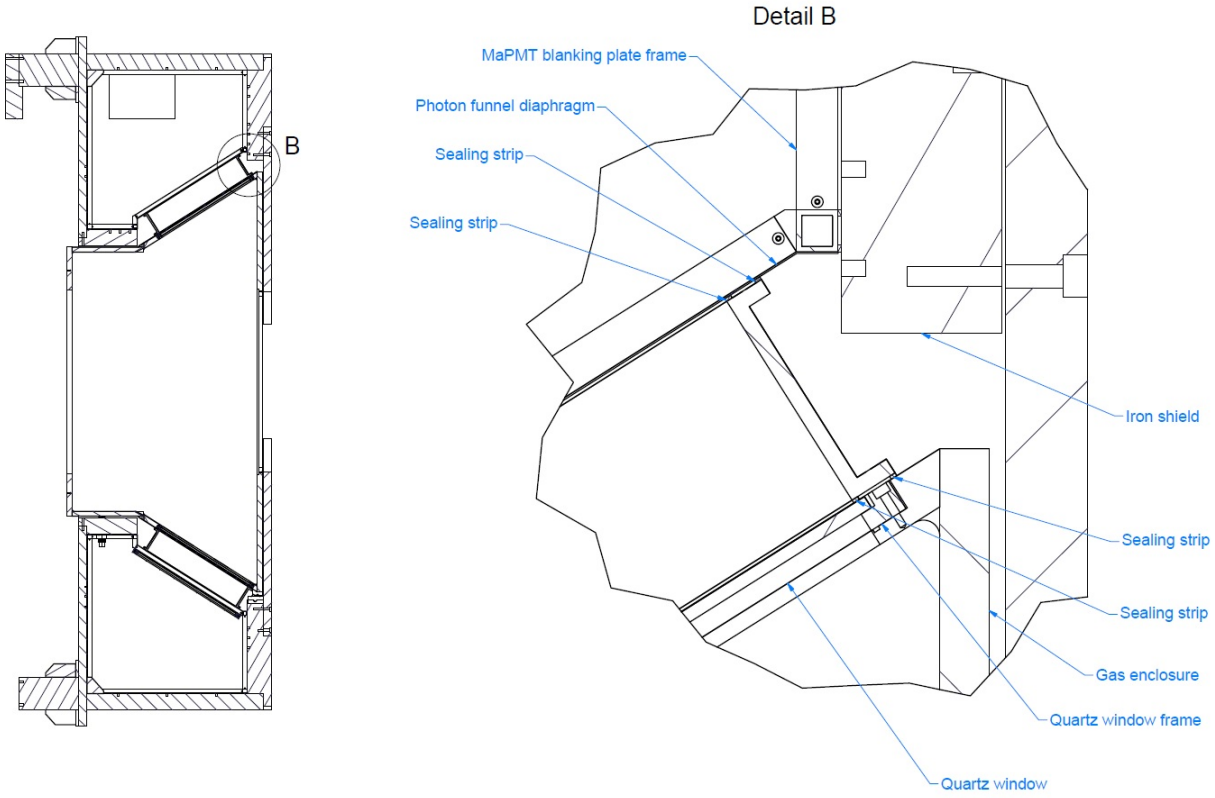


Figure 10: Details of the photon funnel interface to the gas enclosure.

The MaPMT enclosure end-panels are constructed as a space frame in aluminium box section 25.4 mm×25.4 mm and 3.2 mm thick. This framework is bolted together and sealed to the iron shielding with a double strip seal as detailed for the photon funnel. This space frame is very rigid as is the gas enclosure and the photon funnel. When the LHCb dipole magnet is turned on the gas enclosure may move relative to the upper iron shielding by up to 1.0 mm in $z$. This is absorbed by a compliant diaphragm constructed in 1 mm thick aluminium sheet on the face of the MAPMT enclosure where it joins the photon funnel. Figure 11 shows the stress and displacement in this diaphragm under this maximum displacement. Peak stress is about 67 MPa which is within acceptable limits for aluminium considering the number of cycles to which it will be subjected. Other materials are being considered for this diaphragm.

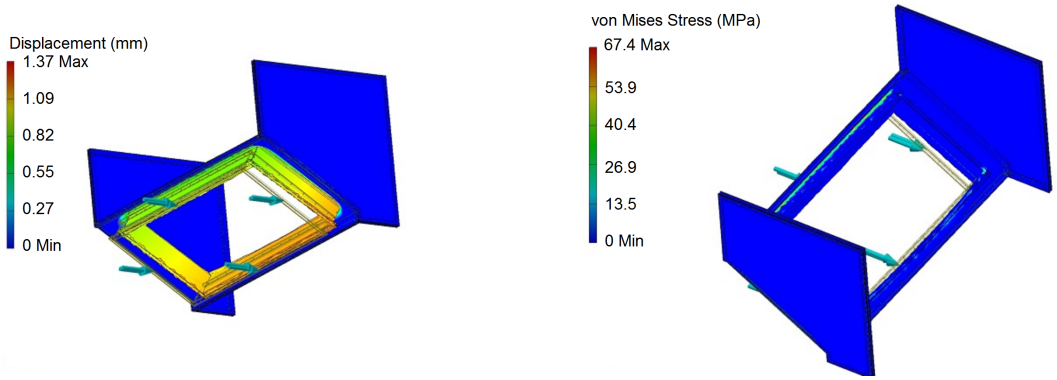


Figure 11: A FEA showing the stress and displacement of the photon funnel diaphragm under maximum displacement.

# 5 The MaPMT region

## 5.1 Introduction and layout

The RICH 1 MaPMT region relies heavily on shared design solutions with RICH 2. The philosophy of having modular systems, i.e. the elementary cells mounted on columns, allows the detector regions of both detectors to be largely similar despite differences in column orientation (horizontal for RICH 1 and vertical for RICH 2). Grouping into common modules has the added advantage of simplifying manufacturing requirements and standardising spare components.

Figure 2 shows a basic overview of the layout for RICH 1. The key differences and similarities for the detector regions of RICH 1, and of RICH 2, are listed below:

- The planes are located directly above and directly below the beampipe for RICH 1, and on either side of the beampipe for RICH 2.
- The access to the modules of RICH 1 is highly restricted, due to a limited working envelope and being enclosed within the magnetic shielding.
- The structural T-pieces which make up the MaPMT columns are the same for both RICHes. However the column mounting and installation mechanisms are different, being dictated by the envelopes and orientation.
- Service routings are more complicated for RICH 1, as dictated by the limited geometry.
- Whilst the elementary cell structure is common to both RICHes, only one type of MaPMT will be used in RICH 1, the Hamamatsu R11265, whereas two types will be used in RICH 2. The electronics readout boards will be the same.
- The cooling concepts, for both liquid coolant and the so-called Levelling Plates are the same for both RICHes. The Levelling Plates couple the electronics to the thermal

block; they cover the digital electronics boards and are machined from aluminium to follow the lines of the chips for optimal thermal coupling.

The geometrical layout of the upgraded RICH 1 resembles the existing detector. There are two planes of MaPMTs, the upper array and the lower array. The upper array is positioned above the beampipe and the lower array is located below. Each array will be formed of 11 columns, shown in Fig. 12. Ten columns are populated with 22 Elementary Cells (ECs), while the column at the upstream end (detecting Cherenkov light from high-angle particles) has 20 ECs. Whilst a column has the potential to accommodate 24 ECs, only 22 are required to cover the acceptance. The 22 ECs are served by six standardised digital readout boards. A summary of the numbers of units is given in Table 1. The dimensions of the MaPMT plane are 621 mm in width and 1230 mm in length, as shown in Fig 4. The two arrays, upper and lower, are tilted towards the planar mirrors at 0.562 rad to the vertical.

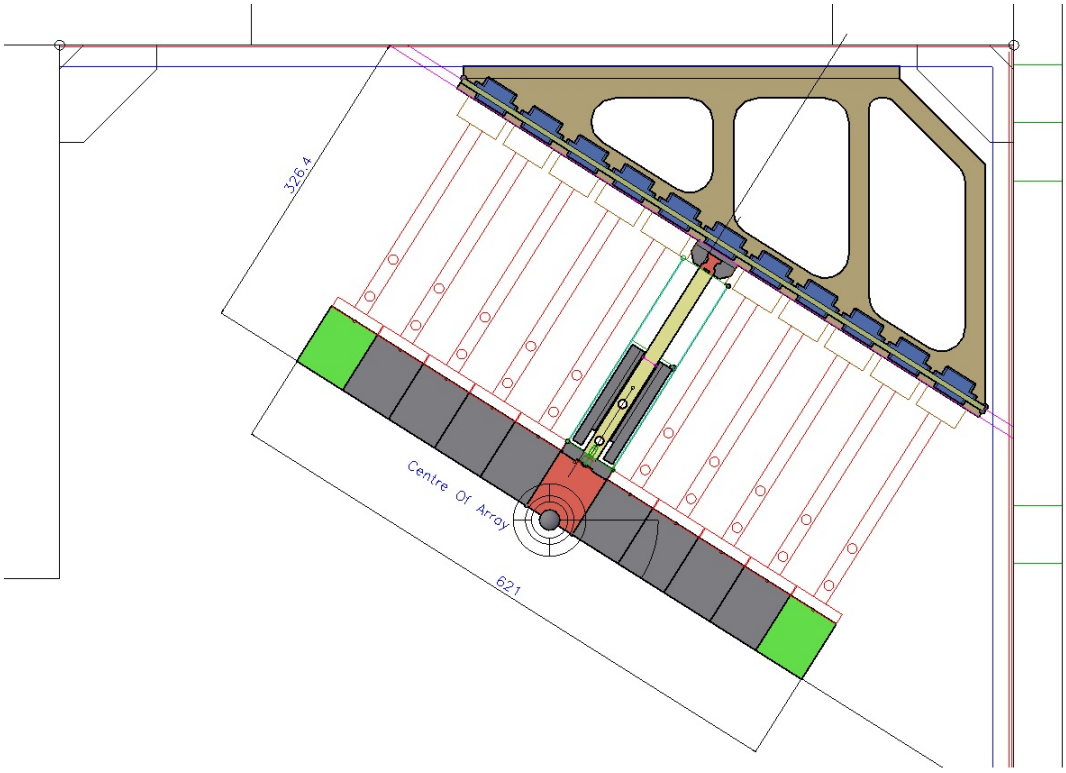


Figure 12: A CAD representation of the upper array. The central column is represented in solid and the remaining columns are shown in outline.

In order to optimise the optical layout, an important objective has been to locate the MaPMT arrays as far back into the corner of the shielding as possible within the fixed envelope of the shielding. The new layout must provide simple and relatively unhindered access, so facilitating efficient and low risk serviceability. This is maximised by adopting modular sub-systems (i.e. a column arrangement).

Table 1: MaPMT and electronics quantities.

| | |
|---|---|
| **For the whole of RICH 1** | |
| Total number of Elementary Cells | (22×10+20×1) ×2 = 480 |
| Total Number of MaPMTs | 480×4 = 1920 |
| **For each array** | |
| Number of columns per array | 11 |
| Modules per column | $5\frac{1}{2}$ (6 pairs of digital boards) |
| Elementary Cells per column | 22(10 off) or 20(1 off) |
| MaPMTs per column | 88(10 off) or 80(1 off) |
| Elementary cells per array | 22×10+20×1 = 240 |
| Total number of MaPMTs per array | 240×4 = 960 |

## 5.2 Support system: the chassis

The support system for each array is called a chassis. The chassis for both upper and lower arrays are close to identical; all functionality and performance is maintained when inverted and only nominal variations are envisaged. The two chassis are robust precision optical benches, and precision machined aluminium-alloy plates form an inclined reference plane. Initial studies indicate that the structures meet the requirements for stiffness yet remain relatively lightweight. The chassis also caters for global alignment of each array when fully populated with columns.

A CAD model of the upper chassis is shown in Fig. 13(left). In this orientation the uppermost plate of the triangular structure will interface directly to the iron shielding, taking advantage of existing holes. The rails on which the MaPMT columns are mounted (slide systems) will interface directly to the underside of the inclined main plate. Stiffening members are added and optimised accordingly. The working system will be a precision bolted assembly.

A stress analysis of the upper chassis is shown in Fig. 13(right). This preliminary analysis was performed on a simplified model, a monolithic structure, and indicates that the stiffness requirements can be met with such a system. The von Mises stress is 3.4 MPa maximum, the maximum deflection is ∼0.10 mm, and the safety factor is >15. It is believed that subsequent iterations can further optimise the stiffness-to-weight ratio.

## 5.3 Assembly and handling considerations

All MaPMT columns are built around a central spine known as a T-piece, shown in Fig. 14 (left). The T-piece is the main structural element for each column and provides a direct reference for the pre-assembled ECs. It is formed of two parts, the base and the spine. It is a precision structure, CNC-machined from aluminium tooling plate and permanently connected with bolts and dowels. The ECs, each of which weighs 0.25 kg, fix directly to the T-piece base. The base of the T-piece is also used to accommodate connectors for elementary cells and digital boards. As described previously, there are eleven columns

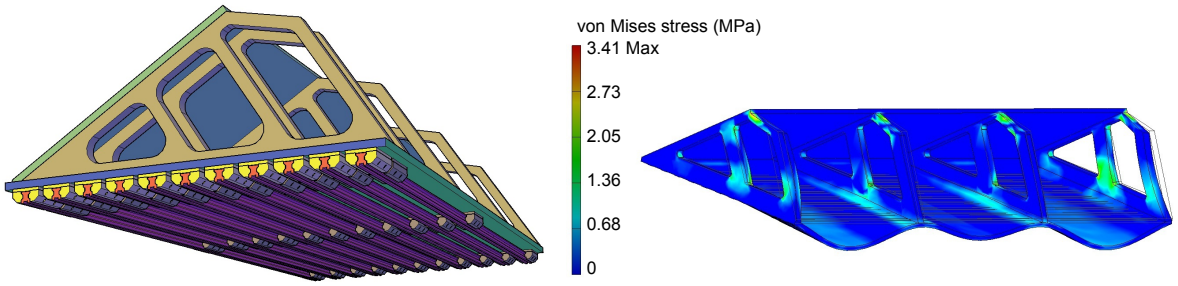


Figure 13: (Left) The upper chassis viewed from the underside. The slide mechanics are shown; the MaPMT frame T-pieces have been omitted. (Right) The deformation (much exaggerated) of the populated chassis. The maximum deflection is ∼0.10 mm. The von Mises stress is colour encoded.

(T-pieces) per array.

The spine of the T-piece is used for the following functions:

- To provide two internal cooling channels, flow and return, connected by a short piping section at the return end.
- To mount the digital boards and their associated levelling plates (which provide thermal connection to the spine and cooling channel).
- To mount the precision slide rail (for mounting to the chassis).
- To mount side enclosures.
- To provide a robust and repeatable support for connectors.

A stress analysis of the T-piece is shown in Fig. 14(right). The preliminary analysis was performed on a simplified model, a monolithic structure. This simplified version indicates that the stability requirements are met and deformation limits are not exceeded. The von Mises stress is 3.92 MPa maximum, the maximum deflection ∼0.147 mm, and the safety factor >15.

In Fig. 14, the precision rail can also be seen on top of the spine, on which the T-piece slides during installation/removal. An assembled column is relatively robust and can be moved and manipulated with a lightweight lifting frame. Each individual column will be fully assembled in workshop/laboratory conditions to minimise risk and maximise quality assurance.

End stops will be included at the ends of the base of the T-pieces. They will be used to fix and locate, via dowels, individual column positions along the $x$-axis. A simple yet robust screw mechanism will provide adjustment. The end stops will only need to be set at the time of initial installation and will be repeatable thereafter.

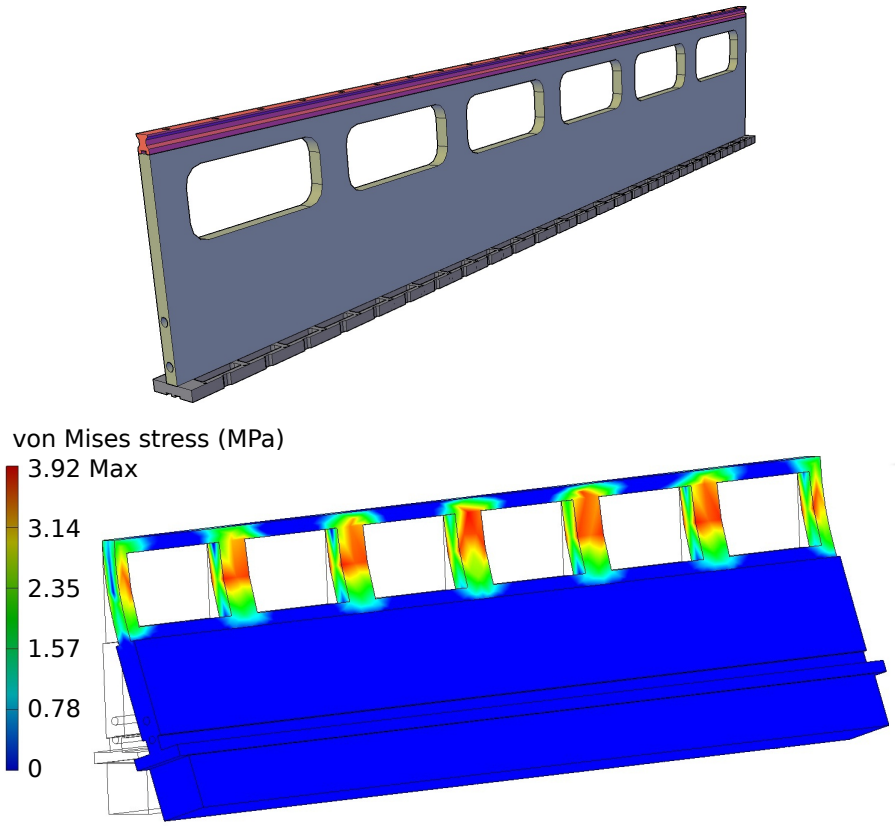


Figure 14: (Top) A CAD drawing of a T-piece, the structural element of an individual column. (Bottom) A stress analysis showing the bending (much exaggerated) of a populated column. The maximum deflection is ∼0.147 mm. The von Mises stress is colour encoded.

## 5.4 MaPMT services, routings and patch panels

The MaPMTs and their readout electronics must be serviced by High Voltage (HV), Low Voltage (LV), data fibres, trigger and control fibres, cooling and additional monitoring cables. All these services are grouped and directed towards their respective patch panels located at the end of the columns in each array. For each MaPMT array there are two main patch panels; one is positioned towards the "C-Side" and one toward the "A-side". The definitions of A- and C-sides are shown in Fig. 15.

The patch panels serve a variety of purposes:

- To support the electrical connectors.
- To allow fibres to pass through.
- To allow cooling to be routed.
- To provide access for the columns.

- To form part of the gas and light tight envelope.

To achieve the gas and light tightness, the panels interface directly with the inside of the shielding plates. The patch panels cater for general access with the addition of appropriately positioned removable plates in the shielding.

The choice of routing is governed by the heights of the existing floors in the cavern, which vary considerably. The higher floor is on the C-side and lends itself to giving better access to the upper array. The lower floor, on the A-side, gives favourable access for the lower array. The upper and lower patch panels have a mirrored inversion. As a result, looking along the beam axis, their equivalent services are routed to opposite sides. LV and HV services are directed to one panel, fibres and cooling are directed to the other, as shown in Fig. 15. The location of the components associated with additional monitoring has yet to be decided.

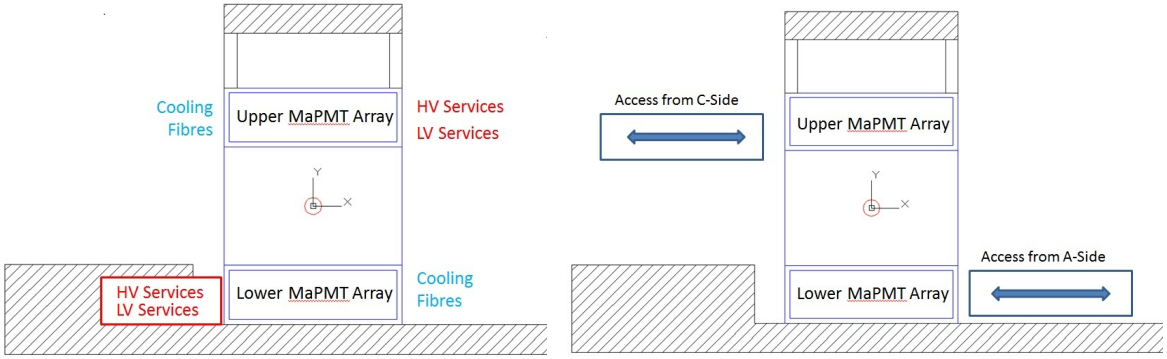


Figure 15: (Left) Plan showing services entering from opposite sides of the detector. (Right) Showing the different floor heights for the A-side and C-side.

The panels that accommodate the LV and HV, shown in Fig. 16, can be considered as permanently closed. When the columns are inserted along their rail system, both the male LV and HV connectors mate "remotely" (i.e. at the opposite end to that at which the column is inserted) with the corresponding female connector located in the panel.

Figure 17(left) shows the routing of LV services along a column from the connectors to the individual digital boards. One connector can accommodate all LV cables for an individual column and all LV services run down one side of a column. Similar to the LV, all HV services will be routed from their respective connectors to the individual ECs. All HV services, shown in Fig 17(right), run down the opposite side of a column to the LV. Again, one connector can accommodate all HV cables for an individual column.

For the fibre services, all fibres will be routed from the individual digital boards along a column towards the connectors, as shown in Fig. 18(left). Because of the 12-way modularity of the fibre bundles, there is a requirement for the fibres to cross from one side of a T-piece to the other, and services will therefore run down both sides of a column. As the fibres reach the end of a column, they are directed upwards towards their own patch panel, shown in Fig. 18(right). Multiple connectors are needed to facilitate the sub-groups of fibres for

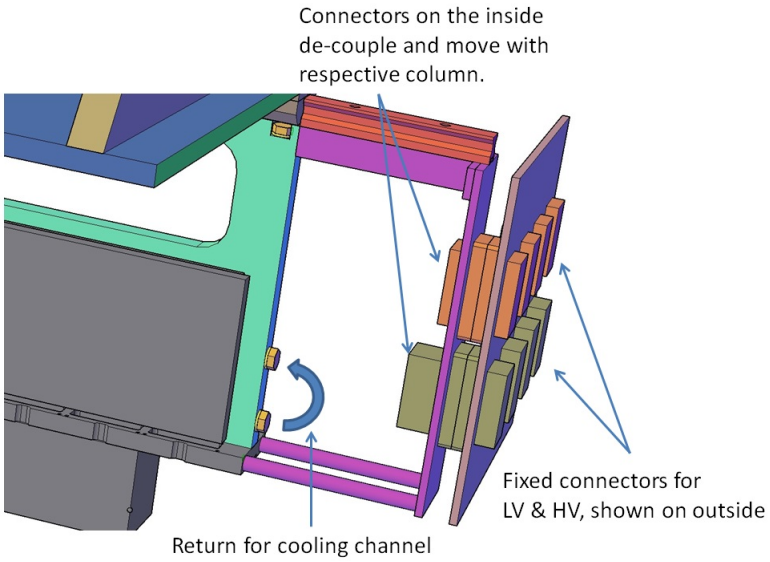


Figure 16: The inside view of a LV and HV patch panel, showing the support from the end of the T-piece.

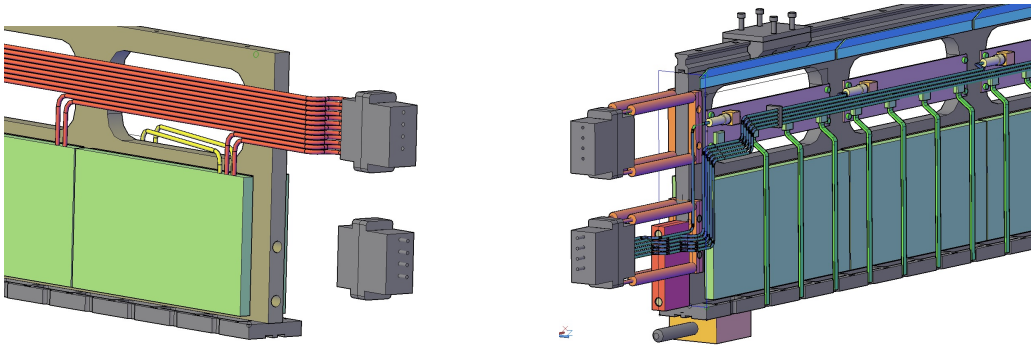

Figure 17: (Left) The LV service routes along a column. The digital board can be seen in green. (Right) The HV service routes in blue, running along a column. Flat cables from the ECs are seen in green (vertical routing).

an individual column. The fibre patch panel sits within the light/gas-tight volume. From there, fibres are regrouped and routed beyond the light-tight enclosure. For fibre, HV and LV routing, extensive CAD modelling of possible routes has been undertaken, including bend radii, fibre diameter, connector access etc.

The cooling channels which are drilled into the spine of the T-piece are two 8 mm diameter holes, one for flow and one for return. A total drill depth of ∼1400 mm is achievable by drilling from either end. Prototype pieces with 10 mm holes have been successfully produced and the tolerances associated with deep drilling are acceptable (<0.5 mm off-axis drift seen at the meeting point). The end holes are visible in Fig. 17(left).

Looking end-on, all pipework and connectors must stay within the envelope of the

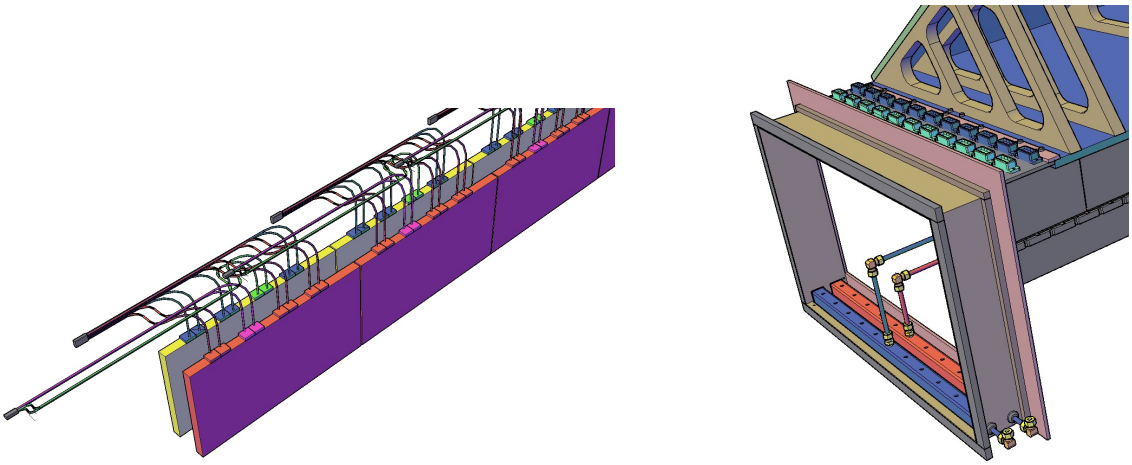

Figure 18: (Left) Typical fibre routing along a column (the T-piece has been omitted from this view). (Right) The fibre connector patch panel, positioned at the end of the chassis base plate (two rows of blue/cyan connectors can be seen).

column that they serve. This allows an individual column to be disconnected and accessed without disturbing its neighbours. The flow and return pipework that projects from the end of a T-piece is routed to distribution manifolds, conceptually illustrated in Fig. 19. Crucially the pipes fit below (above) the extent of the MaPMTs for the upper (lower) array. In the figure the end access panel is seen, together with a smaller green panel. The latter panel allows additional access to the fibre feed-throughs at the time of initial assembly and commissioning.

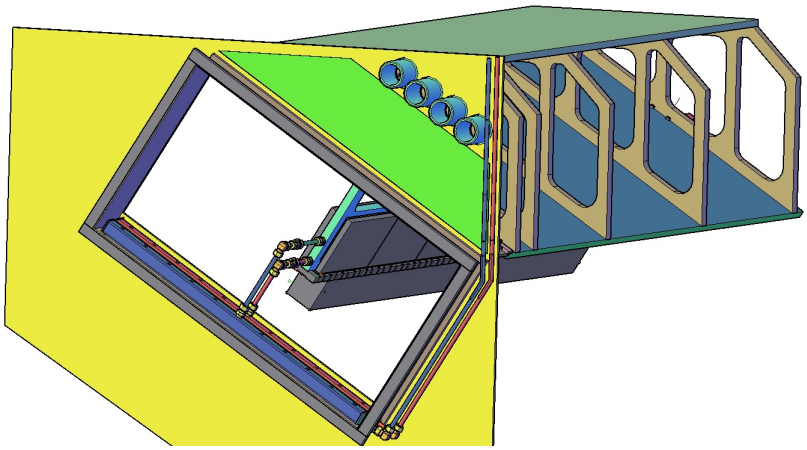

Figure 19: The cooling manifolds shown within the access panel, not obstructing column access.

# 6 Exit window and seal to beam pipe

The arrangement of the new RICH 1 exit window is similar to the current system [4], but due to the change in geometry, a new exit window must be manufactured. The exit window is a low-mass composite panel made from two 0.5 mm thick carbon fibre reinforced epoxy skins separated by 16 mm thick polymethacrylimide (PMI) foam. Each skin is made from two layers of balanced-weave laminate, with fibres orientated to give a 0° / 90° in one layer overlapped with ±45° in the other layer. This is in order to generate skins with as close to uniform a stiffness in the plane as possible. The window will be attached to the downstream face of the RICH 1 gas enclosure using a direct clamping arrangement. This will mean that the alignment of the window will follow that of the gas enclosure. Around the edge of the window, outside the acceptance, is an aluminium retaining ring. This ring gives strength and also provides a surface for sealing. The seal between the gas enclosure and the window will be made on the aluminium retaining ring with an O-ring. In order to minimise the amount of material in the LHCb acceptance, the centre of the window has been tapered at an angle of 30° with respect to the flat. This is the maximum taper that allows for the mirrors to have sufficient clearance for alignment. The details of this tapering arrangement are shown in Fig. 20. Based on the FEA analysis of the current RICH 1 exit window the maximum deflection resulting from a 3 mbar over or under pressure in the gas enclosure will not exceed 5 mm.

The seal to the beam pipe will be made of silicone rubber in a compliant annular shape. The design allows for the window to be isolated from the beam pipe both mechanically and electrically. This will also allow for a ±2 mm misalignment in the exit window. At the outer edge there will be a hook arrangement in the skins of the window. This will be formed from both skins, together giving a 1 mm thickness for strength at this point. The seal will pull over this hook with an incorporated O-ring arrangement. At the inner edge the seal will have a slit to be pushed over the flange in the beam pipe, as in the current arrangement.

The thickness and radiation lengths of the RICH 1 exit window materials are presented in Table 2.

The seal to the VELO (entrance window) will be re-used. In the unlikely event this seal is damaged during dismantling of the current RICH, then the seal will be re-manufactured. All the moulds and materials are available from the current system at RAL.

Table 2: The thickness and radiation lengths of the RICH 1 exit window materials. (Data are taken from Ref. [4].)

| Material | Thickness (mm) | Thickness on angle (mm) | $X0$ (mm) | $\%X0$ along normal | $\%X0$ on angle |
|---|---|---|---|---|---|
| CFRP Laminate | 1.0 | 1.15 | 284 | 0.35 | 0.40 |
| Rohacell 5 IG | 16.0 | 18.48 | 7954 | 0.20 | 0.23 |
| Epoxy Glue | 0.4 | 0.46 | 357 | 0.11 | 0.13 |
| Total | | | | 0.66 | 0.76 |

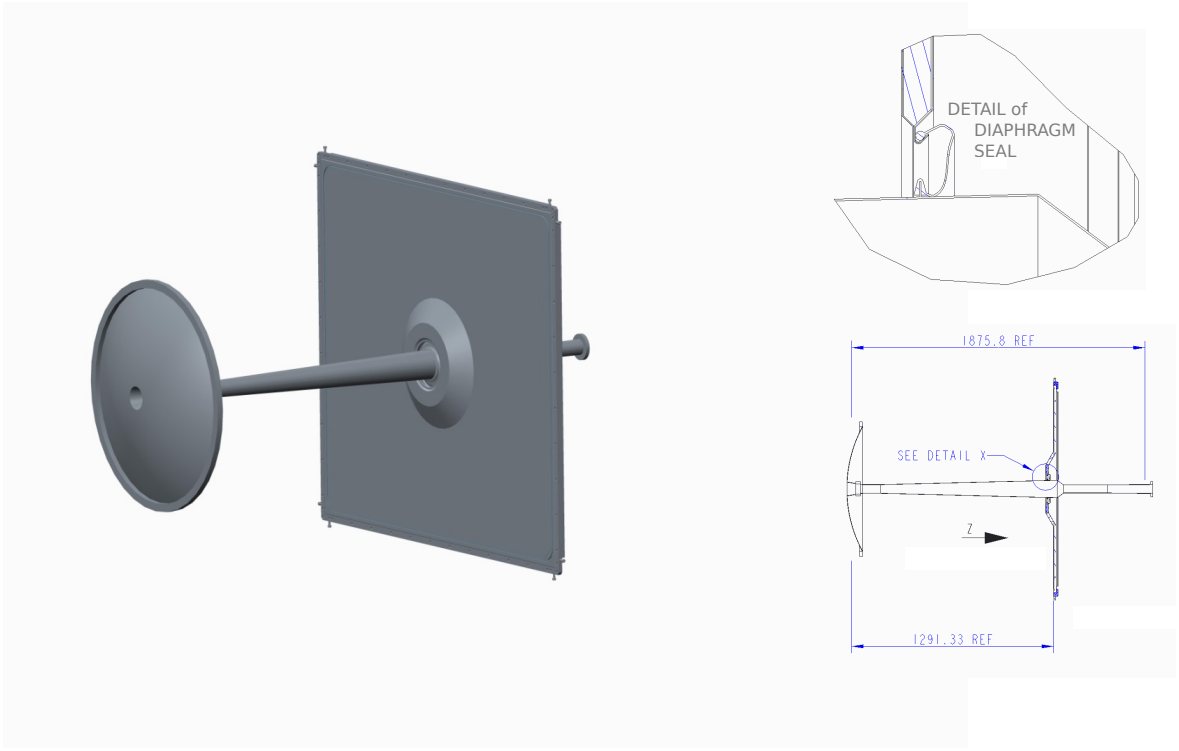


Figure 20: (Left) The exit window and the 25 mrad section of the beam pipe. The current window dimensions in $(x, y)$ are 1604 mm $\times$ 1370 mm, (Right) Detail showing the tapered section of the window, with silicone rubber diaphragm seal to the beam pipe.

# 7 RICH 1 installation and alignment

The dismantling of the current RICH 1 detector will proceed from May - August 2019. No details of this operation are presented here and the reader is referred to Ref. [7]. The general installation process of the upgraded RICH 1 will begin and finish in May 2020. Following installation, the individual components and the RICH 1 detector as a whole will need to be aligned and surveyed in order to correlate the spatial photon hit measurements with the tracking detectors of LHCb. Furthermore the spherical and flat mirror segments need to be pre-aligned accurately in order to form smooth and continuous surfaces.

The RICH 1 detector can be classified, in terms of metrology, in four subsystems:

- The magnetic shielding.
- The gas enclosure.
- The optical system.
- The photon detector assemblies.

The lower magnetic shielding is anchored on the floor and the upper is supported from the cavern wall, and the two parts are not mechanically coupled. Due to the magnetic field, the bottom shield moves about 0.3 mrad (translation along the beam $z$ axis of $\sim$0.5 mm) [8]. The top shield moves slightly less. The gas enclosure is fixed to the bottom shield only. The optical elements include the spherical and flat mirrors. The spherical mirror wall is held at the bottom of the gas enclosure. The flat segments are mounted on two rigid supports which are assembled on the upstream wall of the gas enclosure. Therefore any movement of the lower shield is directly propagated to these optical elements. The two photon detector arrays are mounted on their respective bottom and top shields.

The alignment and survey phases are summarised as follows:

1. The new magnetic shelves will have lifting eyes to be used with the original rail for the gas enclosure. The holes for the chassis which hangs and supports the MaPMT columns will be drilled. The two magnetic shields will be surveyed after the new shelves have been replaced (see Section 2). As no fiducial points have been integrated on the shield, an adapted support compatible for a standard target will be prepared (hole diameter 8 mm [9]). Based on this measurement, the supports for the gas enclosure will be prepared accordingly. The support structures for the MaPMTs will be bolted into the respective magnetic shields prior to the gas enclosure installation.

2. The gas enclosure will be assembled with the quartz windows on the pit floor. The mirror mounts will be attached. The gas enclosure will be installed and then surveyed. Adjustment of its position will be carried out in order to locate it within $\pm$1 mm of its nominal position. The gas enclosure will include fiducial points or have tapped holes for this purpose. At this stage the bellows to couple the gas enclosure to the VELO will be installed and the 25 mrad beampipe section crossing RICH 1 will be mounted to the downstream face of the VELO.

3. After having fed the membrane seal over the beampipe, the exit window will be mounted, which will need to be centred on the beampipe within $\pm$2 mm.

4. Bake out of the beampipe is expected to start February 2020.

5. Mounting and alignment procedure of the optical elements:

   (a) As described in Section 3, the spherical mirror quadrants will be aligned before installation. Their alignment will be performed using a point light source placed at the nominal centre of curvature and a camera to observe the superposition of the reflected spots. A similar method was previously adopted [10]. This pre-alignment is preferably done in the LHCb cavern to minimise the risk of misalignments during transport.

   (b) The flat mirror segments will also be pre-assembled and aligned separately. The alignment of the flat mirror segments will be carried out using a theodolite. The principle consists to target with the theodolite its own image by tilting the

mirror segments. The procedure is repeated for each segment and will give an angular precision of the segment of $\sim$0.1 mrad [11].

(c) The spherical mirror (in two sections) and flat mirror walls (in four sections) will then be installed inside the gas enclosure. Using fiducial marks on the periphery of these assemblies, the mirror frames will be positioned in the LHCb system. Experience from mounting the existing mirrors demonstrates that a positioning accuracy of about 0.5 mm or 1 mrad can be expected [12].

(d) The side panels of the gas enclosure will be installed.

6. The photon detector arrays will be installed inside the upper and lower magnetic shielding. With the installation frame attached to the dowel holes in the shielding, external rails will be matched to the internal chassis rails. The columns will be handled manually onto their assembly rails. The support of the columns will be prepared according to the previous survey of the magnetic shielding. When the columns will be mounted it is intended to survey but not to align them. The positions of the centre of the MaPMT columns need to be known within $\pm$2 mm.

7. Finally the shielding doors will be installed to close up the detector.

# 8 Project planning

The following lists indicate the institutes responsible for delivery of the various work packages and their required completion dates.

1. Shielding: Lead institute: RAL, Critical dates: PRR Apr 2017, installed in time for magnet measurements with shields Aug 2019.

| | | |
|---|---|---|
| 1.1 Main dimensions defined | Imperial | Completed |
| 1.2 Magnetic performance | Imperial | Apr 2017 |
| 1.3 Mechanical design of shelf & mounting points | RAL | Apr 2017 |
| 1.4 Production drawings | RAL | Apr 2017 |
| 1.5 PRR | CERN/RAL | Apr 2017 |
| 1.6 Tender | CERN/RAL | July 2017 |
| 1.7 Production | CERN/RAL | May 2018 |
| 1.8 Installation | CERN/RAL | Aug 2019 |

2. Gas Enclosure: Lead institute: Oxford, Critical dates: PRR Apr 2017, begin assembly May 2019, ready for installation Aug 2019.

| | | |
|---|---|---|
| 2.1 Main dimensions of gas enclosure defined | Oxford | Completed |
| 2.2 Gas enclosure and interfaces final design | Oxford | Nov 2016 |
| 2.3 Photon funnel final design | Oxford | Nov 2016 |
| 2.4 MaPMT end panels design | Oxford | Nov 2016 |
| 2.5 Production drawings and PRR | Oxford | Apr 2017 |
| 2.6 Tender | Oxford | July 2017 |
| 2.7 Production of above | Oxford | May 2018 |
| 2.8 Assembly of all components | Oxford | Aug 2019 |
| 2.9 Installation | CERN/Oxford/RAL | Sept 2019 |

3. Spherical Mirrors, carbon fibre, CMA: Lead institute: Bristol, Critical dates: PRR Apr 2017, order production mirrors July 2018, assembly tests Feb 2020, installation Apr 2020.

| | | |
|---|---|---|
| 3.1 Define final parameters | RAL/Imperial/CERN | Completed |
| 3.2 Prototype testing | Bristol/CERN | Apr 2017 |
| 3.3 PRR including support structure | Bristol | Apr 2017 |
| 3.4 Tender and order production mirrors | Bristol/Oxford/CERN | July 2017 |
| 3.5 Reflective coating | CERN | July 2019 |
| 3.6 Test production mirrors | Bristol/CERN | July 2019 |
| 3.7 Assembly and alignment | Bristol/CERN | Feb 2020 |
| 3.8 Installation | Bristol/CERN/RAL | Apr 2020 |

4. Flat Mirrors, glass: Lead institute: Bristol, Critical dates: PRR Apr 2017, order production mirrors July 2018, assembly tests Jan 2020, installation Apr 2020.

| | | |
|---|---|---|
| 4.1 Prototype testing | Bristol/CERN | Apr 2017 |
| 4.2 PRR including support structure | Bristol | Apr 2017 |
| 4.3 Tender and order production mirrors | Bristol/Oxford/CERN | July 2017 |
| 4.4 Reflective coating | CERN | July 2019 |
| 4.5 Test production mirrors | Bristol/CERN | July 2019 |
| 4.6 Assembly and alignment | Bristol/CERN | Feb 2020 |
| 4.7 Installation | Bristol/CERN/RAL | Apr 2020 |

5. MaPMT assemblies: including mounting frame,columns and cooling assemblies. The column structure and cooling system are shared closely with RICH 2, Lead institute: Imperial, Critical dates: PRR Apr 2017, MaPMT support ready to receive modules May 2018, installation May 2020.

| | | |
|---|---|---|
| 5.1 MaPMT mounting frame - final design | CERN/Imperial/Padova | Nov 2016 |
| 5.2 MaPMT mounting assembly and rail structure | Imperial | Nov 2016 |
| 5.3 Cooling system design | CERN/Imperial/Padova | Nov 2016 |
| 5.4 Patch panels | CERN/Imperial | Nov 2016 |
| 5.5 Production drawings and PRR | Imperial | Apr 2017 |
| 5.6 Tender | Imperial | July 2017 |
| 5.7 Production | Imperial | May 2018 |
| 5.8 Install cooling system | CERN/Imperial | Mar 2020 |
| 5.9 Assembly and alignment | CERN/Imperial | Jan 2020 |
| 5.10 Installation | CERN/Imperial/RAL | May 2020 |

6. Quartz Windows: Will use identical technology to current RICH 1, Lead institute: Oxford, Critical dates: PRR Apr 2017, procurement May 2018, installation Oct 2019.

| | | |
|---|---|---|
| 6.1 Production drawings and PRR | Oxford | Apr 2017 |
| 6.2 Tender | Oxford | July 2017 |
| 6.3 Procurement | Oxford | May 2018 |
| 6.4 Anti-reflective coating | CERN | Oct 2018 |
| 6.5 Gluing | CERN/Oxford | Jan 2019 |
| 6.6 Installation | CERN/Oxford/RAL | Sept 2019 |

7. VELO seal and exit window: The VELO seal is not expected to be replaced, only if damaged. The exit window will be based on the current RICH 1 manufacture. Lead institute: RAL, Critical dates : PRR Apr 2017, Assembly tests Aug 2019, Installation Sept 2019.

| | | |
|---|---|---|
| 7.1 Exit window PRR | RAL | Apr 2017 |
| 7.2 Exit window manufacture | RAL | May 2018 |
| 7.3 Assemble | RAL | Aug 2019 |
| 7.4 VELO seal : manufacture only if necessary | RAL | Sept 2019 |
| 7.5 Installation | CERN/RAL | Sept 2019 |

8. Monitoring, alignment, radiation environment.

| | | |
|---|---|---|
| 8.1 Mirror alignment | Bristol/CERN | July 2019 |
| 8.2 Metrology | CERN | Apr 2020 |
| 8.3 Detector safety interlocks | CERN | Apr 2020 |
| 8.4 Radiation test coordination | CERN | Ongoing |

9. Handling tools: Lead institute: RAL, Critical dates: As required for installation of magnetic shelf at IP8: Jan 2019, as required to execute assembly tests : Aug 2019, as required to facilitate installation at IP8: Sept 2019.

| | | |
|---|---|---|
| 9.1 Magnetic shelf handling | CERN/RAL | Jan 2019 |
| 9.2 External handling structure to access and maintain MaPMTs | Imperial/RAL | Jan 2019 |
| 9.3 Installation procedures for MaPMT columns | CERN/Imperial/RAL | Jan 2019 |
| 9.4 Tools for insertion /removal of spherical mirrors | Bristol/RAL | Sept 2019 |
| 9.5 Tools for insertion/removal of plane mirrors | Bristol/RAL | Sept 2019 |
| 9.6 Tools for insertion and sealing exit window | RAL | Sept 2019 |

A delivery schedule and milestones for the RICH 1 mechanics project are shown in the Gannt chart of Fig. 21.

# Acknowledgments

We would like to thank M. Fiorini of the University of Ferrara for his work on the RICH 1 radiation studies.

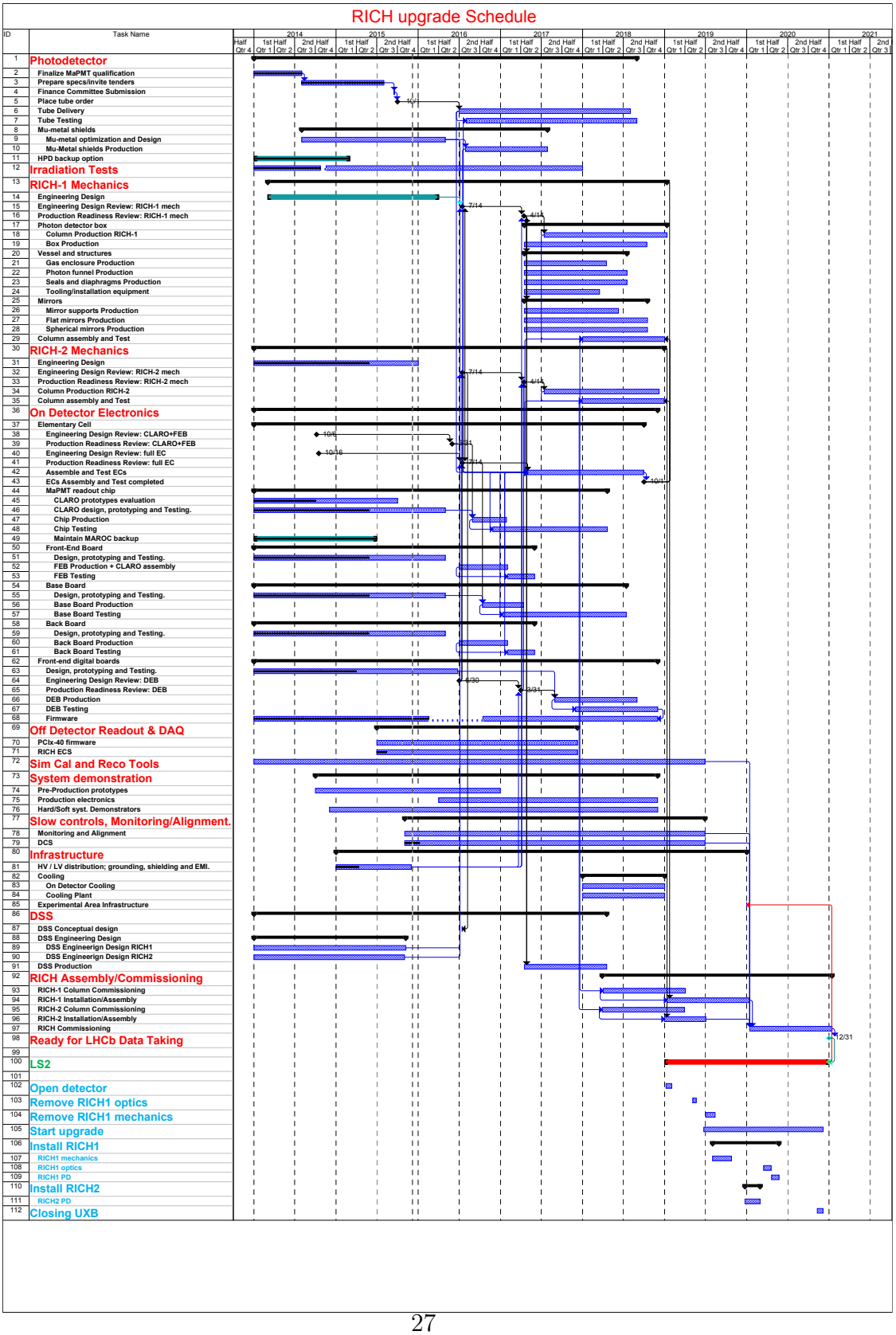




Figure 21: The RICH upgrade project delivery schedule.

# Appendices

## A Appendix A: Cooling requirements

The front-end (FE) electronics system of RICH 1 will dissipate substantial heat, estimated at 6.9 kW, and it is necessary to have an active cooling system. The heat power generated by all active components of RICH 1 photon detector assembly (PDA) is summarised in Table 3. To ensure no degradation of the MaPMT photocathode and to avoid high dark-count rates it is required that the temperature of the photon detectors is maintained below 35 °C. The main heat sources, the electronics components (FPGA, VTX/GBT and DC-DC converters), will be coupled to the cooling bar (T-pieces) via the Levelling Plate (described in Section 5. The target is that these electronics elements will be maintained below 50 °C. In order to achieve a low temperature gradient along the column and at a moderate flow, the permissible coolant temperature elevation is 5 °C. The cooling system is fully described in Ref. [13], and only the requirements of RICH 1 are addressed here.

Table 3: RICH 1 heat power of the front-end electronics.

| Component | Power |
|---|---|
| Digital Boards, LV (7 V, 3.4 A): | 6 kW |
| Front-end ASIC Boards (0.128 W/board) | 250 W |
| The high voltage divider boards | 650 W |
| Total power per Column | 311 W |
| Total power | 6.9 kW |

The proposal is to use a fluid in liquid mono-phase that flows through the MaPMT column. An inert coolant such as a fluorinated fluid is preferred. This would avoid some of the risks associated in cooling the photon detector columns with a water-based system. The use of a fluorinated coolant also allows an implementation of the cooling system similar to the existing one. The cooling plant is located on the safety side of the LHCb cavern (RB84), at the same location of the present unit. Novec$^{TM}$ 649 (Fluoroketone) or Novec$^{TM}$ 7100 (Hydrofluoroether) produced by 3M Corporation are potential replacement coolants of the current perfluorocarbon $C_6F_{14}$. More details on the coolant can be found in Ref. [14]. Whether or not the existing cooling plant could be re-used or upgraded is still being studied.

The target is to maintain a leak rate below 0.05 litres per day. The flow rate will be at least 1750 l/h for each RICH 1 loop, and the pressure drop inside the detector (input to output) will be $\sim$0.7 bar. This pressure drop includes all fittings, manifolds, quick-release connectors, etc.

Table 4 summarises the main requirements of the cooling system for RICH 1.

Table 4: Requirements of the RICH 1 cooling system.

| | |
|---|---|
| Number of circuits (loops): | 2 |
| Nominal heat power: | $2 \times 3.45\,\mathrm{kW}$ |
| Max. temperature of the photon detectors: | $< 35\,^{\circ}\mathrm{C}$ |
| Max. temperature of electronics | $< 50\,^{\circ}\mathrm{C}$ |
| Coolant: | Fluorinated fluid: 3M Novec$^{\mathrm{TM}}$ 649, 7100 or $C_6F_{14}$ |
| Heat transfer medium: | Liquid mono-phase |
| Minimum temperature at the PDA inlet: | $\sim 11\,^{\circ}\mathrm{C}$ |
| Temperature difference of the coolant (PDA outlet), $\Delta T$: | $5\,^{\circ}\mathrm{C}$ |
| Maximum pressure at the PDA inlet: | $< 2\,\mathrm{bar}$ |
| Pressure drop in the PDA: | $\sim 0.7\,\mathrm{bar}$ |
| Leak rate, in total: | $< 0.05\,\mathrm{l/day}$ |
| Typical flow of the coolant: | $1750\,\mathrm{l/h}$ |

# B Appendix B: Radiation hardness

The upgraded LHCb detector will be exposed to a considerable dose of radiation that will strongly depend on the position with respect to the interaction point and to other materials producing secondary particles. All components of the LHCb RICH system that are potentially sensitive to radiation damage (photodetectors, electronics, optical and mechanical parts, interconnections, etc.) have to pass radiation hardness tests in order to ensure stable operation over the expected LHCb lifetime. It is foreseen that the LHCb experiment will accumulate 50 fb$^{-1}$ over 10 years after the upgrade, and all numbers quoted in this Appendix refer to this total integrated luminosity.

Simulations of the radiation levels in the LHCb experiment are performed using FLUKA [15]. Results are available with reasonable statistics for most locations around the experiment and are given in terms of Total Ionising Dose (TID), 1 MeV neutron equivalent fluence per cm$^2$, and High Energy Hadrons >20 MeV (HEH) fluence per cm$^2$. Geometry and materials used in the simulations for RICH 1 are as for the current LHCb: no modifications of RICH 1 mechanics and optics is implemented. Typical statistical errors of 10-30% are assumed on the numbers presented here. As a general assumption, for a specific region corresponding to a well defined RICH component, the worst case value of the corresponding radiation distribution is considered.

From the simulations, in the photodetector region of RICH 1, we should expect a total ionising dose of 2 kGy, a neutron fluence of $3\times10^{12}$ 1 MeV $n_{eq}$/cm$^2$ and a HEH fluence of $1.2\times10^{12}$ cm$^{-2}$ [16]. At the downstream end of RICH 1 the expected average TID is about 140 kGy between 4 cm and 6 cm radial distance from the beam, and decreases to about 80 kGy in the region between 7 cm and 8 cm [17]. In the region $2.5 < x < 5$ cm and

$0 < y < 2.5\,\text{cm}$, the 1 MeV neutron equivalence fluence is about $2\times10^{14}$ cm$^{-2}$, while the HEH fluence is about $4\times10^{14}$ cm$^{-2}$.

The RICH 1 components must survive the above doses, and an initial inventory of components to be irradiated has been identified [18] and listed in Table 5. For each component to be tested, a minimal set of identical samples should be tested before and after irradiation for measurement of the most important parameters that might be degraded during radiation exposure. In addition, one sample should be kept as reference and not irradiated. A safety factor of at least two in radiation levels with respect to the values shown in Table 5 will be used for radiation testing. Whenever possible the components will be tested separately, however for specific parts (for example, interconnections) the radiation hardness of the composite system will be assessed.

Table 5: List of materials to be irradiated and the corresponding expected radiation levels.

| Item | Radial position w.r.t beam | TID [kGy] | HEH [$\times10^{12}$/cm$^2$] | 1 MeV $n_{eq}$ [$\times10^{12}$/cm$^2$] | Tests to be performed |
|---|---|---|---|---|---|
| Gas enclosure sealing (Blue Hylomar) | MaPMT region | 2 | 1.2 | 3 | Pressure, visual, adhesion |
| Exit window, bonding | 12 cm | 40 | 100 | 120 | Tensile test |
| Membrane, material | 6 cm | 100 | 160 | 300 | Tensile test |
| Spherical mirror, bonding | 12 cm | 40 | 100 | 120 | Tensile test on adapted specimen, coupon reflectivity |
| Quartz windows | MaPMT region | 2 | 1.2 | 3 | Optical transmission |
| Bonding of mirrors to support | 30 cm | 8 | 14 | 40 | Tensile test |
| Electrical connectors | MaPMT region | 2 | 1.2 | 3 | Visual, electrical connectivity |

# References


[1] The LHCb Collaboration, "Framework TDR for the LHCb Upgrade : Technical Design Report", CERN-LHCC-2012-007 ; LHCb-TDR-12.

[2] The LHCb Collaboration, "LHCb PID Upgrade Technical Design Report", CERN-LHCC-2013-022 ; LHCB-TDR-014.

[3] M. Adinolfi et al., "Performance of the LHCb RICH detector at the LHC", Eur. Phys. J. C 73 (2013) 2431.

[4] N.H. Brook et al., "LHCb RICH1 Engineering Design Review Report", LHCb EDR 2004, EDMS-493831 29 August 2004.

[5] "Engineering Design Report for the Elementary Cell of the RICH photon detector", EDMS-1627008

[6] L. Cadamuro et al, "Characterization of the Hamamatsu R11265-103-M64 multi-anode photomultiplier tube", JINST 9 (2014) P06021.

[7] C. Frei, "RICH Infrastructure", EDMS-1683369

[8] "Geometrical control during magnet test, BCAM measurements", EDMS-1034892.

[9] C. Lasseur,"Various survey supports : sockets and brackets", EDMS-318084.

[10] C. Frei, "Positions of the lenses and targets used to align the mirrors", EDMS-594541.

[11] S. Berni, "LHCb Hall 156 RICH1 Upper flat mirrors adjustment in clean room June 2007", EDMS-857711.

[12] J-C Gayde, " RICH 1 Position of the Mirrors, March 27 2009", EDMS-993523.

[13] C. Frei, "Cooling investigations for the RICH upgrade", EDMS-1627009.

[14] "Comparison of liquid coolants suitable for single-phase detector cooling." https://twiki.cern.ch/twiki/pub/LHCb/C6K/Coolants-review.pdf

[15] M. Karacson, "Radiation levels in the LHCb cavern", Presentation at the "LHCb Upgrade Electronics" Meeting, February 2013, https://indico.cern.ch/event/225746/

[16] M. Fiorini, "Plans for CLARO8v3 irradiation", Presentation at the "Meeting on Irradiations for RICH Upgrade", February 2016, https://indico.cern.ch/event/503375/

[17] M. Karacson, "Update on expected dose and fluence for the upgraded RICH", Presentation at the "Meeting on Irradiations for RICH Upgrade", February 2016, https://indico.cern.ch/event/503375/

[18] C. Frei, "RICH Upgrade Irradiation", Presentation at the "Meeting on Irradiations for RICH Upgrade", February 2016, https://indico.cern.ch/event/503375/